

Bistability and metastability scenario in the dynamics of an ellipsoidal particle in a sheared viscoelastic fluid

G. D'Avino*

Dipartimento di Ingegneria Chimica, dei Materiali e della Produzione Industriale, Università di Napoli Federico II, P.le Tecchio 80, 80125 Napoli, Italy

M. A. Hulsen

Department of Mechanical Engineering, Eindhoven University of Technology, Eindhoven 5600 MB, The Netherlands

F. Greco

Istituto di Ricerche sulla Combustione, Consiglio Nazionale delle Ricerche, P.le Tecchio 80, 80125 Napoli, Italy

P. L. Maffettone

Dipartimento di Ingegneria Chimica, dei Materiali e della Produzione Industriale, Università di Napoli Federico II, P.le Tecchio 80, 80125 Napoli, Italy and Center for Advanced Biomaterials for Health Care@CRIB, Istituto Italiano di Tecnologia, Largo Barsanti e Matteucci 53, 80125 Napoli, Italy

(Received 24 December 2013; revised manuscript received 31 January 2014; published 7 April 2014)

The motion of an ellipsoidal particle in a viscoelastic liquid subjected to an unconfined shear flow is addressed by numerical simulations. A complex dynamics is found with different transients and long-time regimes depending on the Deborah number De (De is the product of the viscoelastic liquid intrinsic time times the applied shear rate). Spiraling orbits toward a log-rolling motion around the vorticity are observed for low Deborah numbers, whereas the particle aligns with its major axis near to the flow direction at high Deborah numbers. The transition from vorticity to flow alignment is characterized by a periodic regime with small amplitude oscillations around orientations progressively shifting from vorticity to flow direction by increasing De . A range of Deborah numbers is detected such that the periodic solution coexists with the flow alignment regime (bistability). A further range of De is found where flow alignment is attained differently for particles starting far from or next to the shear plane: in the latter case, very long transients are found; hence an effective bistability (metastability) is predicted to occur in a large time lapse before reaching the fully aligned state. Finally, the computed Deborah number values for flow alignment favorably compare with available experimental data.

DOI: [10.1103/PhysRevE.89.043006](https://doi.org/10.1103/PhysRevE.89.043006)

PACS number(s): 47.20.Ky, 82.70.Dd, 47.11.Fg, 47.50.-d

I. INTRODUCTION

The motion of nonspherical particles suspended in fluids is of great relevance in industrial applications and biological systems. For instance, elongated rigid particles are added into fluids to confer special final properties to the composite material [1–4]. Also, shape anisotropy of bioparticles such as bacteria [5–7], microswimmers [8], sperm cells [9], platelets [10], and heterocell aggregates [11] imparts peculiar dynamical properties to the overall flowing materials.

For the case of unconfined shear flow, Jeffery predicted the dynamics of a single, rigid, non-Brownian ellipsoidal particle in a Newtonian fluid [12]. The orbits described by the particle orientation vector (the so-called Jeffery's orbits) are closed periodic curves around the vorticity axis, i.e., the axis orthogonal to the shearing plane. Those predictions found later confirmation in experiments (e.g., [13]).

Particles (both passive and active) are often immersed in fluids that are non-Newtonian (e.g., polymer-filled materials [4,14], spermatozoa swimming through the viscoelastic cervical mucus [15], bacteria in cross-linked polymer gels [16]). The complexity of the suspending liquid strongly alters the observed particle dynamics with respect to that with

a Newtonian fluid in analogous flow conditions. Experiments, indeed, have evidenced that an elongated particle in a sheared viscoelastic liquid at small shear rates drifts across the Jeffery's orbits, and its major axis eventually aligns along the vorticity direction (the so-called log-rolling motion) [17,18]. On the other hand, by increasing the shear rate, a transition from vorticity to flow alignment is found [19,20]. Along with those two limiting regimes, seemingly stable intermediate orientations between vorticity and shearing direction have also been observed [17,19]. A complete and recent experimental work [21] deals with a dilute suspension of ellipsoidal particles (with aspect ratios ranging from 2 to 8) in several non-Newtonian fluids. Optical microscopy images clearly showed the transition from vorticity to flow alignment for increasing shear rates. The critical conditions for the alignment of the ellipsoids along the flow direction at high shear rates have been measured. In a range of intermediate shear rates, however, bimodal orientational distributions were reported, although the achievement of a true steady state could not be confirmed. The two coexisting preferred orientations are either close to vorticity or close to flow direction.

An asymptotic theory [22] in the limiting case of an infinitely elongated particle immersed in a specific non-Newtonian liquid ("second-order fluid", see Ref. [23]) captures the spiraling motion toward the vorticity axis at small shear rates along with the alignment to the flow direction at higher

*gadavino@unina.it

shear rates. On the other hand, no theoretical predictions are available for more realistic particles (i.e., with finite aspect ratios) and/or non-Newtonian fluids, to describe the observed complex dynamics far from the two limiting (log-rolling and flow-aligning) cases.

Numerical works dealing with the motion of nonspherical particles in viscoelastic fluids are quite limited. The slow settling of an ellipsoid through a quiescent viscoelastic liquid (second-order fluid) has been studied by the fictitious domain method [24]. The forces and torques acting on the particle have been calculated in this paper, but actual dynamics of the particles (i.e., trajectories) is not. The rotation of an ellipsoid in a viscoelastic fluid subjected to shear flow has been investigated by a double layer boundary integral method [25]. An Oldroyd-B model [23] is considered as the constitutive equation for the liquid. The simulation results for an aspect ratio equal to 2 and Deborah number $De = 0.7$ (the Deborah number is defined as the product of the fluid relaxation time and the applied shear rate) show the slowing down of the rotation period as well as the tendency of the particle to spiral toward the vorticity axis. However, as remarked by the authors, the large amount of CPU time limits the simulations to few rotation periods, small Deborah numbers, and low particle aspect ratios.

The aim of this work is to use direct numerical simulations to investigate the detailed dynamics of a nonbuoyant anisotropic particle in a sheared viscoelastic liquid. Numerical results for particle aspect ratios ranging from 1 (sphere) to 16, for different Deborah numbers and initial orientations, are presented. A comparison with the available theories and experimental data is carried out.

II. GOVERNING EQUATIONS

The investigated system is sketched in Fig. 1. A single ellipsoidal particle is located between two parallel plates moving at equal but opposite velocities (simple shear flow). We denote with a and b the semimajor and semiminor ellipsoid axes, and we denote with $AR = a/b$ the aspect ratio. The distance between the two plates W is much larger than a so as to represent an unconfined system. A Cartesian reference frame is centered at the particle center of mass, and x , y , and z axes are the flow, gradient, and vorticity

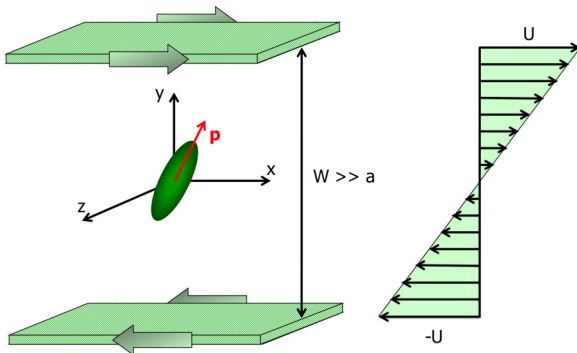


FIG. 1. (Color online) Schematic representation of the problem investigated in this work. On the right, the generated flow field without the particle (simple shear flow) is reported.

directions, respectively; i.e., the imposed velocity field far from the ellipsoid is $\mathbf{u}_\infty = (u_x, u_y, u_z) = (\dot{\gamma}y, 0, 0)$, with $\dot{\gamma}$ being the shear rate. The particle orientation is described by the orientation pseudovector \mathbf{p} that identifies the direction of the ellipsoid major axis.

By neglecting both fluid and particle inertia, the fluid motion is governed by the continuity and the momentum balance equations:

$$\nabla \cdot \mathbf{u} = 0, \quad (1)$$

$$\nabla \cdot \boldsymbol{\sigma} = \mathbf{0}, \quad (2)$$

where \mathbf{u} is the fluid velocity and $\boldsymbol{\sigma}$ is the total stress tensor, expressed as

$$\boldsymbol{\sigma} = -p\mathbf{I} + 2\eta_s\mathbf{D} + \boldsymbol{\tau}. \quad (3)$$

In Eq. (3), p , \mathbf{I} , η_s , and $\mathbf{D} = (\nabla\mathbf{u} + (\nabla\mathbf{u})^T)/2$ are the pressure, the unity tensor, the viscosity of a Newtonian “solvent”, and the rate-of-deformation tensor, respectively. Finally, $\boldsymbol{\tau}$ is the viscoelastic stress tensor that needs to be specified by choosing a constitutive equation. In this work, as the constitutive equation we consider the Giesekus model [23] that, despite its simplicity, has been proven to quantitatively describe the rheological properties of several non-Newtonian fluids [26–28]:

$$\lambda \overset{\nabla}{\boldsymbol{\tau}} + \frac{\alpha\lambda}{\eta_p} \boldsymbol{\tau} \cdot \boldsymbol{\tau} + \boldsymbol{\tau} = 2\eta_p\mathbf{D}. \quad (4)$$

In this equation, η_p is a viscosity, λ is the fluid relaxation time, the symbol $(\overset{\nabla}{\boldsymbol{\tau}})$ denotes the upper-convected time derivative

$$\overset{\nabla}{\boldsymbol{\tau}} \equiv \frac{\partial \boldsymbol{\tau}}{\partial t} + \mathbf{u} \cdot \nabla \boldsymbol{\tau} - (\nabla\mathbf{u})^T \cdot \boldsymbol{\tau} - \boldsymbol{\tau} \cdot \nabla\mathbf{u}, \quad (5)$$

and α is a (dimensionless) constitutive parameter. We recall that the Giesekus model predicts, in simple shear flow, viscosity thinning with increasing the shear rate for any value of the constitutive parameter α greater than zero. In addition, such a model predicts both nonzero first and second normal stress differences, $N_1 = \sigma_{xx} - \sigma_{yy}$ and $N_2 = \sigma_{yy} - \sigma_{zz}$. (The existence of normal stresses in shear is the “fingerprint” of a viscoelastic liquid.) Finally, we also recall that the limiting case $\alpha = 0$ in Eq. (4) corresponds to the well-known Oldroyd-B model and that, for small values of the Deborah number [see Eq. (9)], the Giesekus model tends to the second-order fluid constitutive equation.

Concerning the boundary conditions, we apply unperturbed shear flow \mathbf{u}_∞ far from the particle. More details on this condition are given in the next section, where the computational domain used in the simulations is discussed. On the particle boundary $P(t)$, the rigid-body motion is imposed:

$$\mathbf{u} = \boldsymbol{\omega} \times \mathbf{r} \quad \text{on } \partial P(t), \quad (6)$$

where \mathbf{r} denotes the position vector of a point on the particle surface and $\boldsymbol{\omega}$ is the angular velocity of the particle (to be determined).

As inertia is neglected, no initial condition for the velocity field needs to be specified. On the other hand, since the time derivative of the viscoelastic stress tensor appears in the constitutive equation, an initial condition for $\boldsymbol{\tau}$ is required.

We assume a stress-free condition, i.e., that the stress is zero everywhere in the fluid at the initial time:

$$\boldsymbol{\tau}|_{t=0} = \mathbf{0}. \quad (7)$$

To close the set of governing equations, the hydrodynamic torque acting on the particle needs to be specified. As inertia is neglected, the particle is torque free; i.e., the total torque \mathbf{T} on the spherical surface is zero:

$$\mathbf{T} = \int_{\partial P(t)} \mathbf{r} \times (\boldsymbol{\sigma} \cdot \mathbf{n}) dS = \mathbf{0}, \quad (8)$$

where \mathbf{n} is the outwardly directed unit normal vector on ∂P .

The solution of the above equations gives the time evolution of the fields \mathbf{u} , p , and $\boldsymbol{\tau}$ and of the unknown $\boldsymbol{\omega}$. Knowledge of the latter quantity allows one to update the particle orientation, i.e., to compute the particle trajectory $\mathbf{p}(t)$. A specific initial orientation is chosen by selecting an initial value $\mathbf{p}|_{t=0} = \mathbf{p}_0$.

It is convenient to make the above equations dimensionless. We select the reciprocal of the imposed shear rate as characteristic time $t_f = \dot{\gamma}^{-1}$, the major semiaxis a as characteristic length, and η_p/t_f as characteristic stress. Then, the Deborah number defined as

$$\text{De} = \lambda \dot{\gamma} \quad (9)$$

appears in all the equations. The Deborah number compares the fluid characteristic time λ and the flow time t_f . The Newtonian liquid response is obtained for $\text{De} = 0$, since the Newtonian liquid has no characteristic time. The dimensionless system of equations contains three dimensionless parameters: α , the viscosity ratio η_s/η_p , and the Deborah number De . Furthermore, the only geometrical parameter is the aspect ratio AR . All the simulations have been performed by selecting $\alpha = 0.2$ and $\eta_s/\eta_p = 0.1$. This particular choice for α denotes a shear-thinning fluid whose rheology fairly describes the liquid with the most complete data set in Ref. [21]. The dynamics of an ellipsoidal particle in a viscoelastic liquid is analyzed for different Deborah numbers and aspect ratios.

III. NUMERICAL METHOD

The above described system of equations is solved by the finite element method. To assure convergent solutions at relatively high Deborah numbers, we implement the Discrete Elastic Viscous Split Stress-G/Streamline Upwind Petrov Galerkin formulation [29–31] together with a log representation for the conformation tensor [32,33]. We recall that the angular velocity $\boldsymbol{\omega}$ is an unknown and needs to be calculated in order to satisfy the torque-free condition Eq. (8). Such a condition is imposed through constraints in each node of the particle surface by means of Lagrange multipliers [34]. In this way, the angular velocity is automatically computed by solving the augmented system of equations.

Once the angular velocity $\boldsymbol{\omega}$ is available, we need to update the orientation of the ellipsoid. This is done by using the quaternion formalism [35]. Quaternions are quadruples of real numbers (q_1, q_2, q_3, q_4) related to the Euler angles. The quaternion formalism provides an easy way to track the orientation of bodies in space [35]. Indeed, it can be shown

that the following relationship holds [35,36]:

$$\begin{pmatrix} \dot{q}_1 \\ \dot{q}_2 \\ \dot{q}_3 \\ \dot{q}_4 \end{pmatrix} = \frac{1}{2} \begin{pmatrix} q_4 & -q_3 & q_2 & q_1 \\ q_3 & q_4 & -q_1 & q_2 \\ -q_2 & q_1 & q_4 & q_3 \\ -q_1 & -q_2 & -q_3 & q_4 \end{pmatrix} \cdot \begin{pmatrix} \omega_x \\ \omega_y \\ \omega_z \\ 0 \end{pmatrix}, \quad (10)$$

i.e., the time evolution of the quaternion is related to the angular velocity $\boldsymbol{\omega}$ through a 4×4 matrix. From the knowledge of quaternion dynamics, we can evaluate the rotation matrix $\mathbf{R}(t)$ [corresponding to the angular velocity $\boldsymbol{\omega}(t)$]:

$$\begin{aligned} \mathbf{R}(t) &= 2 \begin{pmatrix} q_1^2 + q_4^2 - 0.5 & q_1q_2 + q_3q_4 & q_1q_3 - q_2q_4 \\ q_1q_2 - q_3q_4 & q_2^2 + q_4^2 - 0.5 & q_2q_3 + q_1q_4 \\ q_1q_3 + q_2q_4 & q_2q_3 - q_1q_4 & q_3^2 + q_4^2 - 0.5 \end{pmatrix}. \end{aligned} \quad (11)$$

$\mathbf{R}(t)$ transforms a vector from the (fixed) laboratory frame to a (time-dependent) frame that follows the ellipsoid:

$$\mathbf{v}(t) = \mathbf{R}(t) \cdot \mathbf{v}_0, \quad (12)$$

with \mathbf{v}_0 being a generic vector in the fixed frame and $\mathbf{v}(t)$ being the same vector in the frame oriented according to the principal axes of the ellipsoid. Notice that the rotation matrix in Eq. (11) is updated every time step. By applying the rotation matrix computed at the current time level $\mathbf{R}(t_{n+1})$ to a vector having initial orientation $\mathbf{v}(t_0)$, we obtain the vector $\mathbf{v}(t_{n+1})$ that is oriented according to a reference frame that followed the ellipsoid dynamics. Specifically, if the vector $\mathbf{v}(t)$ is the direction $\mathbf{p}(t)$ of the ellipsoid major axis, we can easily compute the particle orientation during the whole simulation. The same formalism will also be applied to rotate the whole simulation mesh (see below).

The computational domain used in our simulations consists of a sphere including the ellipsoid and with its center coinciding with its barycenter. The choice for such a domain is convenient for the reasons explained below. We divide the space between the spherical surface and the ellipsoid in tetrahedral elements with smaller elements close to the ellipsoid where larger gradients are expected. The unperturbed shear flow boundary conditions are then applied on the spherical surface. Results of the computations will become independent from the sphere radius for R_{out} much larger than the ellipsoid major axis a . Notice that, due to the applied boundary conditions, some regions of the spherical surface are inflow sections and the stress tensor needs to be specified. On the nodes belonging to those sections, we set the stress values computed for the same fluid used in the simulations, subjected to shear flow without any particle and taken at the same instant of the simulation time. In this way, we assume that, far from the particle, the viscoelastic stress field is the unperturbed one; i.e., we apply far-field boundary conditions for both velocity and stresses.

To account for the particle motion, we adopt the arbitrary Lagrangian-Eulerian moving mesh method [37]. According to this method, the mesh follows the particle motion and the internal nodes are updated by solving a Laplace equation

for the mesh velocity [37]. The computed mesh velocity \mathbf{u}_m is, then, subtracted from the convected terms appearing in the governing equations. Since inertia is neglected, the only convective term is present in the upper-convective time derivative Eq. (5). As the elements become more and more distorted, after some steps, remeshing should be performed and the solution on the old mesh would need to be projected on the new one. For the system under investigation, however, we can rigidly rotate the whole mesh by following the ellipsoid dynamics. In this way, the relative distance between the node elements does not change and no distortion occurs, avoiding remeshing and projection steps. Therefore, at each time step, we apply Eq. (12) to all the mesh nodes \mathbf{x}_m . The mesh velocity \mathbf{u}_m is computed from the node positions \mathbf{x}_m by using a first-order Euler scheme for the first time step and a second-order backward differencing for the second and further steps. As the computation proceeds, the nodes of the external boundary rotate as well. The choice of a spherical domain easily allows us to compute the inflow nodes where the unperturbed stress tensor needs to be applied. Further details on the time discretization of the constitutive equation, the weak formulation, and the adopted solver can be found elsewhere [38].

Spatial and temporal convergence as well as the adequateness of the domain size in order to assure unperturbed flow far from the particle are checked for all the calculations presented in this work. We conclude this section by giving some information about the computational times. The CPU time required for a simulation is strongly affected by the aspect ratio and the Deborah number. High values of those parameters limit the maximum time step size to be used. In addition, high aspect ratios correspond to large rotation periods and, consequently, require large integration times to fully describe the particle orbit. A typical simulation to compute the orbit for an ellipsoid with aspect ratio $AR = 2$ and $De = 4$ initially released out of the xy plane requires about 2–3 days of CPU time. For an ellipsoid with $AR = 16$ (the maximum explored in this work) the computational time increases to 2–3 weeks.

IV. RESULTS

We proceed by illustrating the detailed dynamics of an ellipsoid with aspect ratio $AR = 4$, which corresponds to the most investigated value in Ref. [21]. For $De = 1$ and an initial particle orientation lying in the gradient-vorticity plane close to the vorticity axis, the orbit described by the orientation vector is reported in Fig. 2(a). A spiraling motion eventually leading to alignment along the vorticity direction is found. Thus, the final regime is the so-called log-rolling motion with the ellipsoid rotating around its axis of revolution that coincides with the vorticity direction. Similar results are found for whatever initial condition of the ellipsoid, out of the shearing plane, as shown in Fig. 2(b) for an ellipsoid initially oriented with its major axis near the gradient direction. When the initial orientation lies within the shear plane, instead, the ellipsoid forever tumbles around the vorticity axis, with its major axis always in the shear plane (see the Appendix).

The situation at a substantially higher Deborah number is shown in Figs. 2(c) and 2(d) ($De = 3$). Starting from the same initial conditions of Figs. 2(a) and 2(b), an initial fast dynamics

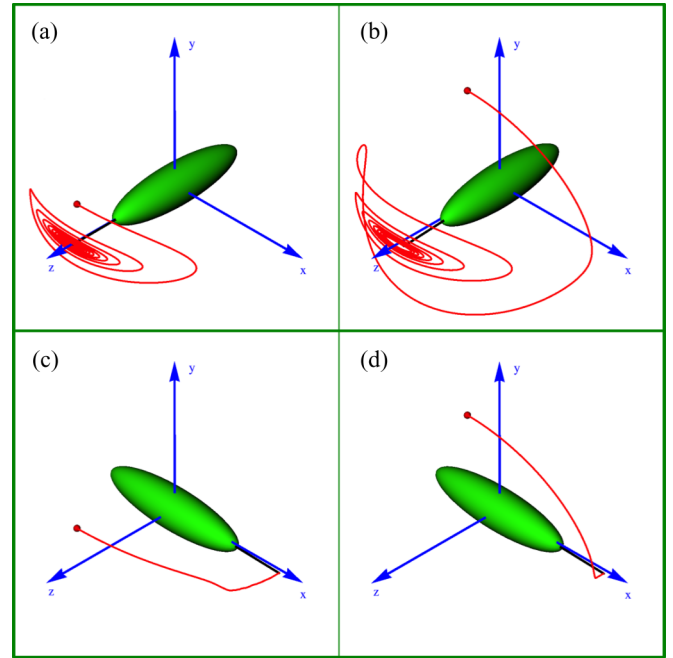


FIG. 2. (Color online) Orbits described by the orientation vector for an ellipsoid with aspect ratio $AR = 4$ and $De = 1$ (a and b) and $De = 3$ (c and d). In the leftmost panels, the initial orientation vector (red circles) is $(p_{x,0}, p_{y,0}, p_{z,0}) = (0, 0.31, 0.95)$ whereas in the rightmost panels it is $(p_{x,0}, p_{y,0}, p_{z,0}) = (0, 0.95, 0.31)$.

of \mathbf{p} is observed toward the flow-vorticity plane, followed by a very slow motion leading to the flow axis. The ellipsoid eventually attains a steady-state regime, with its major axis aligned within the shear plane, and very close to the flow direction (in fact, slightly below it). Such a final regime is found for any initial condition, including those with the initial orientation within the shear plane (see the Appendix).

Those simulation results correctly capture the experimentally observed transition from vorticity to flow alignment moving from low to high Deborah numbers. As mentioned above, a change in the orientation direction from log-rolling motion to flow alignment had been previously predicted for slender bodies [22]. We would like to note, however, that our computed final orientation at high shear rates lies in the flow-gradient plane but is slightly below the flow direction, at variance with the theoretical prediction (i.e., the major axis exactly along the flow axis). Such a difference can be ascribed to the finite aspect ratio used in our calculations. Other simulations carried out at larger aspect ratios indeed confirm that the orientation vector approaches the flow axis for progressively more elongated particles.

Through numerical simulations we are capable of investigating the *intermediate* De range by following the ellipsoid dynamics throughout, up to the long-time regimes. In Fig. 3, the particle dynamics for $De = 2.2$ (a–c), $De = 2.5$ (d–f), and $De = 2.7$ (g–i), for the same initial positions close to the vorticity (left columns) and gradient (central columns) directions, are reported. For all the investigated Deborah numbers, by releasing the particle near the vorticity direction, the orientation vector initially moves toward the flow axis approaching the flow-vorticity plane, then inverts its direction

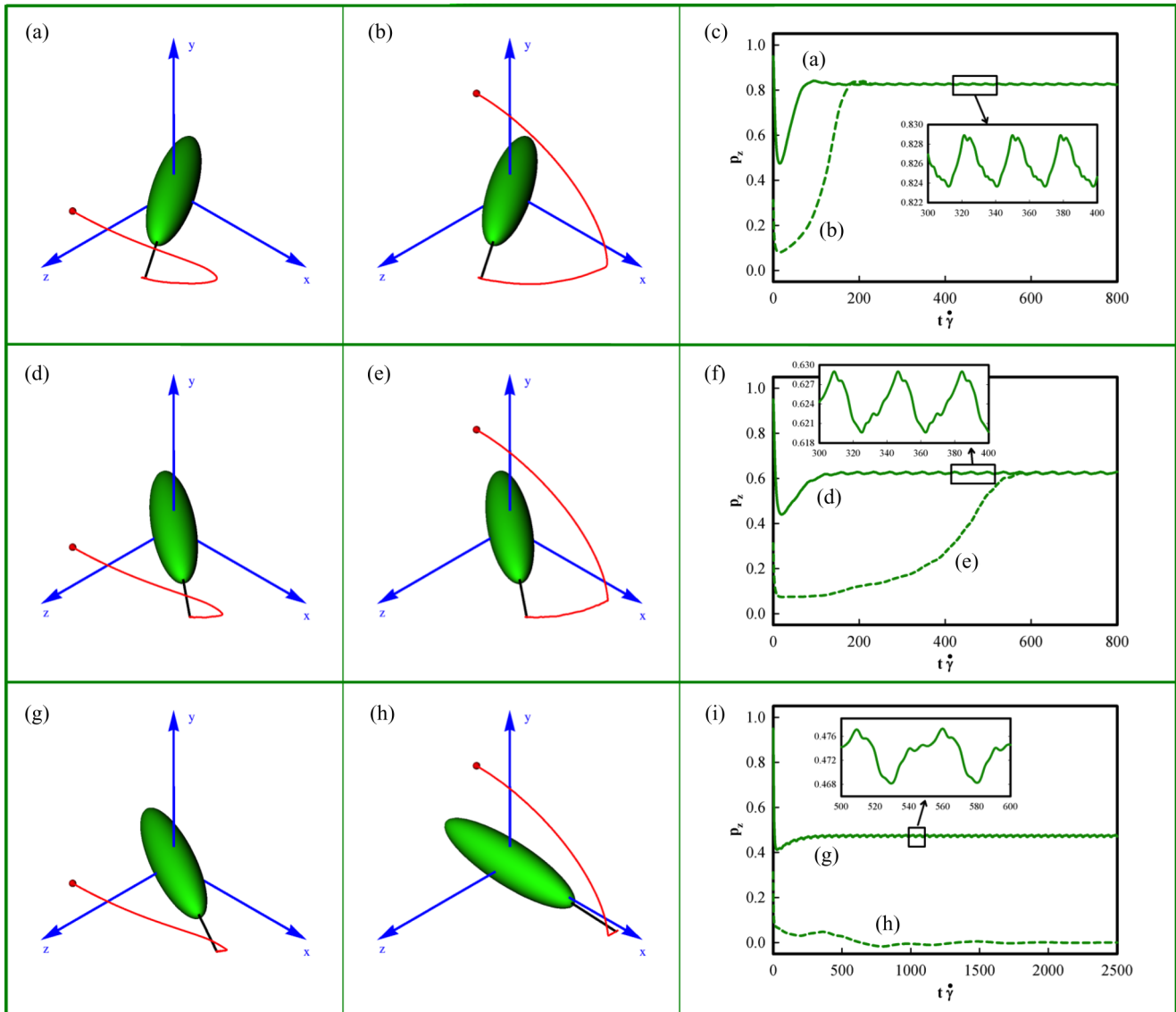


FIG. 3. (Color online) Orbits described by the orientation vector for an ellipsoid with aspect ratio $AR = 4$ and $De = 2.2$ (a–c), $De = 2.5$ (d–f), and $De = 2.7$ (g–i). In the leftmost panels, the initial orientation vector (red circles) is $(p_{x,0}, p_{y,0}, p_{z,0}) = (0, 0.31, 0.95)$ whereas in the central panels it is $(p_{x,0}, p_{y,0}, p_{z,0}) = (0, 0.95, 0.31)$. In the rightmost panels, the time evolution of the z component of the orientation vector corresponding to the orbits in the left and central columns is reported. Insets: The details of the oscillations over a time window of 100 dimensionless units.

moving back toward the vorticity, and finally stops at an equilibrium position in between the x and z axis. The final orientation is closer to the flow axis for increasing Deborah number values. Actually, a closer inspection of the orbits described by the orientation vector at long times shows the existence of small amplitude periodic oscillations. Such a periodic regime is clearly visible in the rightmost column of Fig. 3, where the time evolution of the z component of the orientation vector is reported as solid lines.

A different scenario occurs for an ellipsoid starting with its major axis close to the flow-gradient plane. The central plots of Fig. 3 show that the ellipsoid orientation vector initially moves toward the xz plane for all three cases. However, whereas for $De = 2.2$ [Fig. 3(b)] and $De = 2.5$ [Fig. 3(e)] the major axis drifts toward the aforementioned periodic regime, for $De = 2.7$ the particle orientation vector tends to the

flow-gradient plane. In other words, for $De = 2.7$, we found the coexistence of two equilibrium orientations, i.e., a periodic regime with oscillations around an orientation in between the flow and vorticity directions, and a steady-state regime with the major axis aligned near the flow direction. The dashed lines in the right column of Fig. 3, corresponding to the orbits just discussed, further clarify the ellipsoid dynamics evidencing the achievement of a different long-time regime for $De = 2.7$.

The complex dynamics just presented can be conveniently represented through the so-called *solution diagram* [39] of our dynamical system (for $AR = 4$) by reporting the long-time particle dynamics as a function of the Deborah number. Indeed, the complete picture of results at various De values is illustrated in Fig. 4. The solution is represented by the z component of the orientation vector of the particle. Only the positive range $(0,1)$ of p_z is plotted, as negative values are

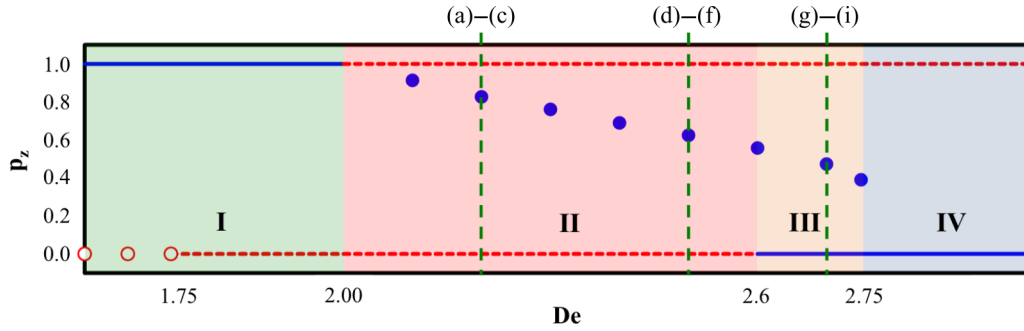


FIG. 4. (Color online) The z component of the orientation vector corresponding to equilibrium regimes as a function of the Deborah number. The solid blue curves denote stable steady-state regimes, the closed blue circles correspond to stable periodic regimes, the horizontal dashed red line refers to unstable steady-state regimes, and the open red circles denote unstable periodic regimes. Four regions corresponding to different behaviors are identified and are denoted by different colors. The vertical dashed lines refer to the orbits reported in Fig. 3.

mirror symmetric with respect to $p_z = 0$. The solid blue curves in Fig. 4 denote stable steady-state equilibrium orientations, whereas the filled blue circles refer to stable periodic solutions. Dashed red lines and empty red circles refer to unstable steady-state and unstable periodic solutions, respectively. In the solution diagram, we can identify four regions characterized by different dynamical behaviors. Regions I and IV are the log-rolling and flow-aligning solutions as discussed above and shown in Fig. 2.

Regions II and III refer to the dynamically rich intermediate De range. We first note that a bistability scenario is predicted in region III, corresponding to the situation in Figs. 3(g)–3(i): Two stable regime solutions coexist, namely, a flow-aligning steady solution and a periodic solution around some $0 < p_z < 1$. Thus, a population of noninteracting ellipsoids observed from the shear gradient direction (as in [21]) in such conditions would show orientations both along the shearing direction and at a certain angle with that direction (actually, two angles symmetric with respect to the shearing direction). Our predictions for the aspect ratio under scrutiny show that the bistability region is rather narrow, however, as it extends from $De = 2.6$ to 2.75 .

By decreasing the De value, we enter region II in the solution diagram, where the steady-state flow-aligning solution becomes unstable: the only stable solution remains the periodic one with average orientation becoming progressively close to the vorticity direction ($p_z = 1$) as De decreases. The orbits in Figs. 3(a)–3(f) belong to such a region. It is worthwhile to mention, however, that, although the particle orientation for De within region II reaches a unique periodic regime at long times, the transients at different De are quite dissimilar. At low De in region II, the final regime is attained in a relatively short dimensionless time [see Fig. 3(c)]. By increasing De still in region II, i.e., getting progressively closer to region III, the orbit starting close to the shear plane remains close to the velocity direction for a substantially large lapse of time [see Fig. 3(f)].

In Fig. 4, some unstable solutions are reported as well. The open red circles at $p_z = 0$ refer to the tumbling motion around the vorticity observed by releasing the ellipsoid with its major axis on the flow-gradient plane. Such a periodic regime becomes steady around $De = 1.75$ (the dashed red line in Fig. 4). As mentioned above, both equilibrium solutions are

unstable (see the Appendix), i.e., small perturbations lead the ellipsoid toward the log-rolling motion or the periodic regime, depending on the Deborah number. Finally, the dashed red line at $p_z = 1$ denotes unstable solutions with the ellipsoid major axis oriented along the vorticity direction. It should be remarked that the reported unstable solutions are not exhaustive. Indeed, at least one more unstable regime is expected to be in region III that divides the periodic and steady-state solutions. Such an unstable regime, however, cannot be detected by time integration and different techniques are required (e.g., parametric continuation [40]).

It so appears that simulations correctly capture the recently observed bimodality in orientational distribution within a range of shear rates for a population of noninteracting ellipsoids in a non-Newtonian fluid [21]. One might argue, however, that the predicted bistability region is indeed quite narrow. In contrast, the above discussed predictions of transients as those reported in Figs. 3(d)–3(f) enlarge the *effective* bistability range, as it is seen that ellipsoids starting close to the shearing plane ($p_{z0} = 0$) spend a considerable amount of time aligned around the flow direction before slowly approaching the unique stable periodic solution. Thus, experiments with limited observation time windows would evidence particles that quickly align between flow and vorticity and particles aligned along the flow. This is coherent with the suspicions of the authors of Ref. [21]: “we cannot be sure that (our findings) represent the true-steady state”.

To sum up, the rich dynamic features in the intermediate De region (regions II and III) somehow connect the two extreme behaviors of a unique attractor along the vorticity as soon as De is switched on and of another unique attractor along the flow direction for high De values; both such attractors were indeed discussed in Ref. [22]. In the intermediate De range, it is as if the mutual attractor strengths were smoothly switched from one to the other, thus promoting a window with periodic solutions. Simulations have been repeated for an aspect ratio $AR = 8$. The same qualitative behavior as for $AR = 4$ is found, with the existence of the four regions depicted in Fig. 4. The general behavior is that the transition between consecutive regions occurs at lower Deborah numbers.

From the data in Fig. 4, we can define a *critical Deborah number* for flow alignment De_{flow} as the lowest De value such that the ellipsoid aligns in the flow-gradient plane, i.e.,

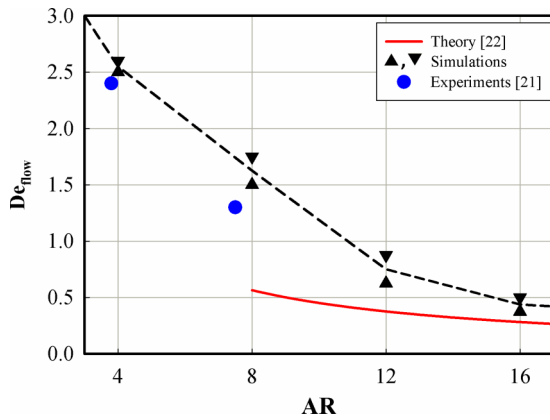


FIG. 5. (Color online) Critical Deborah number for flow alignment as a function of the aspect ratio. The lower (upper) triangles are the minimum (maximum) simulated values such that flow alignment is a stable (unstable) solution. The dashed line passes through the average value of the lower and upper triangles and serves as guide for the eye. The solid red curve is the theoretical prediction in Ref. [22]. The closed blue circles are experimental data taken from Ref. [21].

the boundary between regions II and III of Fig. 4. For an aspect ratio $AR = 4$, we find $De_{\text{flow}} = 2.6$. By repeating the simulations for different aspect ratios, we observe that De_{flow} decreases for more and more elongated particles. We report the computed values in Fig. 5 as lower triangle symbols. The upper triangles in the same figure refer to the maximum simulated Deborah numbers such that the flow axis is an unstable solution regime. Therefore, the exact critical Deborah number value for alignment near the flow direction lies in between the upper and lower triangles. By taking the average values, we obtain the dashed black line in Fig. 5 as a guide for the eye. In the same figure, we add the theoretical predictions from Ref. [22] (the solid red line). The constitutive parameters used for the second-order fluid to draw the red line are selected such that, at vanishing Deborah numbers, the same rheological properties of our Giesekus model are reproduced. Recalling that the theory assumes small Deborah numbers and very high aspect ratios, the solid red curve starts to be valid at the lower-right part of the diagram. Hence, it is not surprising that strong discrepancies are observed for low aspect ratios (corresponding to relatively high critical Deborah numbers), whereas the two trends get closer and closer for more elongated particles (and correspondingly lower De_{flow}). Finally, the blue circles in Fig. 5 are the critical Deborah numbers taken from the experiments in Ref. [21]. An aqueous solution of Polyethylene Oxide with a molecular weight of 4×10^6 g/mol was used as the suspending liquid, with rheological properties that are fairly described by the Giesekus model with the constitutive parameters considered in this work. A fair quantitative agreement between experimental data and numerical predictions is found.

V. CONCLUSIONS

In summary, we have investigated the dynamics of an ellipsoidal particle in a sheared non-Newtonian fluid by numerical simulations. Our results reveal a complex scenario

with different behaviors depending on the Deborah number. The transition from vorticity to flow alignment is characterized by a rich intermediate regime, with alignment in between the vorticity and flow direction with small amplitude periodic oscillations. A bistability range of De values is detected with two stable orientations (region III). A further *metabistability* range of De values is also found, with very long transients for ellipsoids starting close to the shear plane (the rightmost part of region II). Finally, the critical Deborah number for flow alignment (the transition from region II to III) favorably compares with experiments. The present study reconciles the various experimental and theoretical observations reported in previous works within an overall picture.

The present findings demonstrate that real particle shape and fluid rheology must be accounted for to obtain realistic results. We infer that similar accuracy in the description of the dynamics will also be required when studying the motion of active particles in complex media. Finally, single-object dynamics of anisotropic particles will have important implications on the bulk rheology of particle-filled suspensions, giving rise to very different non-Newtonian overall properties depending on the actual orientational states.

APPENDIX: THE SPECIAL CASE OF AN ELLIPSOID INITIALLY ORIENTED ON THE FLOW-GRADIENT PLANE

The dynamics of an ellipsoid initially oriented with its major axis on the flow-gradient plane is here presented. In this condition, the angular velocity vector ω has only one nonzero component (rotation around the vorticity direction) that is denoted by ω . Furthermore, because of the symmetry, the ellipsoid major axis always lies on the xy plane. Notice also that the initial orientation is irrelevant as, after the start-up due to the viscoelastic stress development, different initial orientations correspond to angular velocity (and rotation angle) trends that are shifted in time.

Simulations are performed for particles with aspect ratios ranging from 1 (sphere) to 16 and for different Deborah numbers. It is found that, after an initial transient due to the stress development, the ellipsoid can tumble around the vorticity direction or attain a steady state with the major axis slightly below the flow direction, depending on the aspect ratio and the Deborah number. For the periodic case, the (normalized) angular velocity averaged over a period $\bar{\omega}$ is calculated. (The average is performed after the initial start-up.) In the case in which a steady state is achieved, we set $\bar{\omega} = 0$. Figure 6 shows $\bar{\omega}$ as a function of the Deborah number for different aspect ratios. It is readily observed that fluid viscoelasticity always slows down the particle rotation, in agreement with previous studies for spherical particles [34]. No steady state is found for $AR = 2$ in the range of Deborah numbers investigated. In contrast, flow alignment is found for $AR = 4$ and beyond a critical Deborah number of $De = 1.75$. By increasing the aspect ratio, the average angular velocity decreases, similarly to the Newtonian case [12] that corresponds to the data on the y axis of the plot. Furthermore,

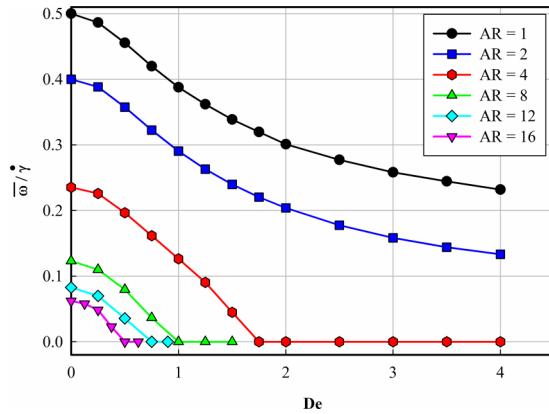


FIG. 6. (Color online) Average angular velocity as a function of the Deborah number for different aspect ratios. An ellipsoid initially released with its long axis on the flow-gradient plane is considered.

the blockage of the ellipsoid near the flow direction is found for smaller Deborah numbers as the particle is more elongated, in agreement with the theoretical predictions [22].

As a final comment, we remark that all the data in Fig. 6 corresponding to the particle flow alignment are equilibrium points. However, from this figure, no indication can be given about the stability of those points because of the very special initial condition of a particle with its long axis lying on the flow-gradient plane. Therefore, due to the symmetry, the particle remains on the xy plane even if the flow alignment condition is an unstable equilibrium point. The analysis of the final stable regime attained by the ellipsoid requires simulations with particles released out of the flow-gradient plane, as those presented in the main text. In this sense, the curves in Fig. 6 are a subset of the full particle dynamics. In particular, the data for $AR = 4$ correspond to the curves in the solution diagram of Fig. 4 for $p_z = 0$.

- [1] L. A. Goettler and K. S. Shen, *Rubber Chem. Technol.* **56**, 619 (1983).
- [2] P. N. Balaguru and S. P. Shah, *Fiber-Reinforced Cement Composites* (McGraw-Hill, New York, 1992).
- [3] S. Varghese, B. Kurlakose, S. Thomas, and A. T. Koshy, *J. Adhes. Sci. Technol.* **8**, 235 (1994).
- [4] C. Bakis, L. Bank, V. Brown, E. Cosenza, J. Davalos, J. Lesko, A. Machida, S. Rizkalla, and T. Triantafyllou, *J. Compos. Constr.* **6**, 73 (2002).
- [5] M. C. Kim and C. Klapperich, *Lab Chip* **10**, 2464 (2010).
- [6] F. D. C. Farrell, O. Hallatschek, D. Marenduzzo, and B. Waclaw, *Phys. Rev. Lett.* **111**, 168101 (2013).
- [7] F. Peruani, Jörn Starruß, V. Jakovljevic, L. Søggaard-Andersen, A. Deutsch and M. Bär, *Phys. Rev. Lett.* **108**, 098102 (2012).
- [8] F. Kümmel, B. ten Hagen, R. Wittkowski, I. Buttinoni, R. Eichhorn, G. Volpe, H. Löwen, and C. Bechinger, *Phys. Rev. Lett.* **110**, 198302 (2013).
- [9] E. A. Gillies, R. M. Cannon, R. B. Green, and A. A. Pacey, *J. Fluid Mech.* **625**, 445 (2009).
- [10] N. A. Mody and M. R. King, *Phys. Fluids* **17**, 113302 (2005).
- [11] H. Ota, T. Kodama, and N. Miki, *Biomicrofluidics* **5**, 034105 (2011).
- [12] G. B. Jeffery, *Proc. R. Soc. London A* **102**, 161 (1922).
- [13] E. Anczurowski and S. G. Mason, *Trans. Soc. Rheol.* **12**, 209 (1968).
- [14] S. Varghese, B. Kuriakose, and S. Thomas, *J. Appl. Polym. Sci.* **53**, 1051 (1994).
- [15] L. J. Fauci and R. Dillon, *Annu. Rev. Fluid Mech.* **38**, 371 (2006).
- [16] J. W. Costerton, K. J. Cheng, G. G. Geesey, T. I. Ladd, J. C. Nickel, M. Dasgupta, and T. J. Marrie, *Annu. Rev. Microbiol.* **41**, 435 (1987).
- [17] E. Bartram, H. L. Goldsmith, and S. G. Mason, *Rheol. Acta* **14**, 776 (1975).
- [18] Y. Iso, D. L. Koch, and C. Cohen, *J. Non-Newtonian Fluid Mech.* **62**, 115 (1996).
- [19] Y. Iso, D. L. Koch, and C. Cohen, *J. Non-Newtonian Fluid Mech.* **62**, 135 (1996).
- [20] S. J. Johnson, A. J. Salem, and G. G. Fuller, *J. Non-Newtonian Fluid Mech.* **34**, 89 (1990).
- [21] D. Z. Gunes, R. Scirocco, J. Mewis, and J. Vermant, *J. Non-Newtonian Fluid Mech.* **155**, 39 (2008).
- [22] L. G. Leal, *J. Fluid Mech.* **69**, 305 (1975).
- [23] R. G. Larson, *Constitutive Equations for Polymer Melts and Solutions* (Butterworth-Heinemann, Boston, 1988).
- [24] J. Feng, D. D. Joseph, R. Glowinski, and T. W. Pan, *J. Fluid Mech.* **283**, 1 (1995).
- [25] N. Phan-Thien and X. J. Fan, *J. Non-Newtonian Fluid Mech.* **105**, 131 (2002).
- [26] A. Calin, N. Wilhelm, and C. Balan, *J. Non-Newtonian Fluid Mech.* **165**, 1564 (2010).
- [27] W. M. H. Verbeeten, *J. Rheol.* **54**, 447 (2010).
- [28] F. Snijkers, G. D'Avino, P. L. Maffettone, F. Greco, M. A. Hulsen, and J. Vermant, *J. Non-Newtonian Fluid Mech.* **166**, 363 (2011).
- [29] R. Guenette and M. Fortin, *J. Non-Newtonian Fluid Mech.* **60**, 27 (1995).
- [30] A. C. B. Bogaerds, A. M. Grillet, G. W. M. Peters, and F. P. T. Baaijens, *J. Non-Newtonian Fluid Mech.* **108**, 187 (2002).
- [31] A. N. Brooks and T. J. R. Hughes, *Comp. Meth. Appl. Mech. Eng.* **32**, 199 (1982).
- [32] R. Fattal and R. Kupferman, *J. Non-Newtonian Fluid Mech.* **123**, 281 (2004).
- [33] M. A. Hulsen, R. Fattal, and R. Kupferman, *J. Non-Newtonian Fluid Mech.* **127**, 27 (2005).
- [34] G. D'Avino, M. A. Hulsen, F. Snijkers, J. Vermant, F. Greco, and P. L. Maffettone, *J. Rheol.* **52**, 1331 (2008).
- [35] D. C. Rapaport, *The Art of Molecular Dynamics Simulation* (Cambridge University Press, New York, 1995).
- [36] Z. Yu and X. Shao, *J. Comp. Phys.* **227**, 292 (2007).
- [37] H. H. Hu, N. A. Patankar, and M. Y. Zhu, *J. Comp. Phys.* **169**, 427 (2001).
- [38] G. D'Avino, T. Tuccillo, P. L. Maffettone, F. Greco, and M. A. Hulsen, *Comput. Fluids* **39**, 709 (2010).
- [39] S. H. Strogatz, *Nonlinear Dynamics and Chaos* (Perseus, Cambridge, 1994).
- [40] E. L. Allgower and K. Georg, *Introduction to Numerical Continuation Methods, SIAM Classics in Applied Mathematics* (Society for Industrial and Applied Mathematics, Philadelphia, 2003).